Tomographic characterisation of gas-jet targets for laser wakefield acceleration

Couperus, J. P.; Köhler, A.; Wolterink, T. A. W.; Jochmann, A.; Zarini, O.;
Bastiaens, H. M. J.; Boller, K. J.; Irman, A.; Schramm, U.;

Originally published:

March 2016

Nuclear Instruments and Methods in Physics Research A 830(2016), 504-509

DOI: https://doi.org/10.1016/j.nima.2016.02.099

Perma-Link to Publication Repository of HZDR:

https://www.hzdr.de/publications/Publ-22627

Tomographic characterisation of gas-jet targets for Laser Wakefield Acceleration

J.P. Couperus[a,b,*], A. Köhler[a,b], T.A.W. Wolterink[c], A. Jochmann[a], O. Zarini[a,b], H.M.J. Bastiaens[c], K.J. Boller[c], A. Irman[a], U. Schramm[a,b]

[a] *Helmholtz-Zentrum Dresden - Rossendorf, Institute of Radiation Physics, Bautzner Landstrasse 400, 01328 Dresden, Germany*
[b] *Technische Universität Dresden, 01069 Dresden, Germany*
[c] *University of Twente, PO Box 217, 7500 AE Enschede, the Netherlands*

Abstract

Laser wakefield acceleration (LWFA) has emerged as a promising concept for the next generation of high energy electron accelerators. The acceleration medium is provided by a target that creates a local well-defined gas-density profile inside a vacuum vessel. Target development and analysis of the resulting gas-density profiles is an important aspect in the further development of LWFA.

Gas-jet targets are widely used in regimes where relatively high electron densities over short interaction lengths are required (up to several millimetres interaction length, plasma densities down to $\sim 10^{18}\,cm^{-3}$). In this paper we report a precise characterisation of such gas-jet targets by a laser interferometry technique. We show that phase shifts down to 4 mrad can be resolved. Tomographic phase reconstruction enables detection of non-axisymmetrical gas-density profiles which indicates defects in cylindrical nozzles, analysis of slit-nozzles and nozzles with an induced shock-wave density step. In a direct comparison between argon and helium jets we show that it cannot automatically be assumed, as is often done, that an nozzle measured with argon will provide the same gas density with helium.

Keywords: Laser wakefield acceleration, LWFA, gas-jet analysis, interferometry, tomography

*Corresponding author. E-mail address: j.couperus@hzdr.de Fax: +49 351 26013005

1. Introduction

Laser wakefield acceleration (LWFA) [1] is a promising concept for the next generation of compact electron accelerators. Using the wakefield created by an ultra-short laser pulse travelling through an underdense plasma, acceleration gradients can be as high as 100 GV/m, three to four orders of magnitudes higher than in conventional RF accelerators. Ever since the first demonstration of LWFA in 1994 [2] the field is quickly developing. Recently generation of Multi GeV electron beams with energies up to 4.2 GeV, 6% rms energy spread and 9 pC charge have been reported by channelling a 0.3 PW ultrashort pulse in a 9 cm long capillary discharge waveguide [3]. However, many challenges in laser wakefield accelerators still remain. Main challenges are on how to improve shot-to-shot energy and pointing stability, energy spread and achievable charge per bunch. For further optimisation of the LWFA process it is crucial to have exact knowledge of the medium in which the acceleration takes place. Besides capillaries, gas-jet targets are the main provider for acceleration media in LWFA. In this paper we present characterisation of such LWFA gas-jet targets by laser-interferometry. For axisymmetrical targets we perform a reconstruction method based on an Abel-inversion algorithm which gives the gas-density distribution. Using helium as a fully ionisable gas, this provides the electron density distribution n_e for LWFA. However, due to the low refractive index of helium gas, interferometric phase shift measurements are challenging. One can rely on the use of higher refractive gases like argon or nitrogen [4–6], but as we show in section 3.2 this does not necessarily represent the exact gas density profile of the same nozzle operated with helium gas. Therefore we use an ultra sensitive interferometric setup in order to perform measurements on helium directly.

Targets providing longer interaction lengths or gas-density steps normally do not posses axisymmetry. For these kind of targets we use a tomographic reconstruction algorithm.

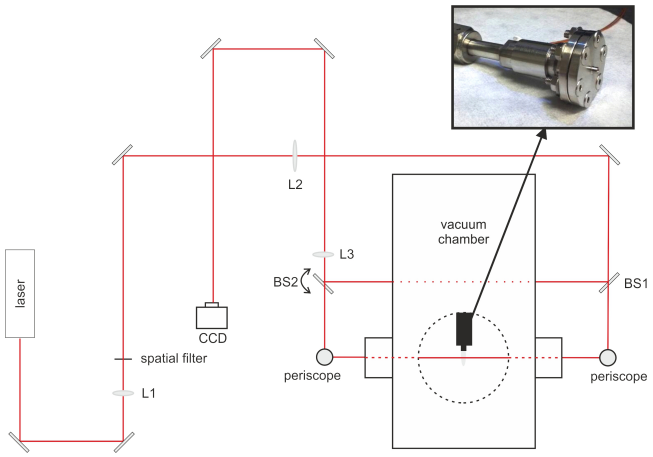

Figure 1: Schematic representation of the gas-jet interferometry setup. Lenses L1 & L2 function as a beam expander. L3 images the target plane onto the CCD. The inset shows a 0.75 mm cylindrical nozzle. For tomography purposes the gas-jet target can be rotated to take measurements under multiple angles.

2. Method of Analysis

2.1. Experimental Setup

In interferometry, the presence of the gas induces an optical path length difference between the probe arm and a reference arm resulting in a phase shift on the interferogram. A schematic of our setup is shown in figure 1. The Mach-Zehnder type interferometer consists of a 18 mW continuous wave HeNe laser at 632.8 nm (Linos G040-814-00 with PS-3170). Depending on the nozzle size, the laser beam is expanded to illuminate the entire gas-jet by lenses L1 and L2 in a telescope configuration. In this telescope we spatially filter the beam using a pinhole to acquire a spatially homogeneous beam. Both interferometer arms have approximately the same length to stay within the coherence length of the laser. 50:50 beamsplitters (BS1 & BS2) are used to achieve the highest interferometric fringe contrast. The arms overlap at a CCD camera (PCO.pixelfy) which is positioned at the image plane of the gas-jet created by lens L3. Temporal resolution is achieved by short (μs range) camera exposure. A small angle

α introduced at BS2 results in a fixed sinusoidal interference pattern along the x-direction according to [7, 8]

$$I = 2I_0 \left[1 + \cos\left(kx \sin\left(\alpha\right)\right)\right], \tag{1}$$

where k=$(2\pi)/\lambda_L$ is the laser wavenumber. This constant pattern acts as the carrier pattern, which is necessary as a carrier for the phase-shift that the gas-jet induces in the signal arm.

The gas-jet in the signal arm introduces an optical path length difference (ΔOPL), which adds to the intensity function which is imaged on the CCD:

$$I = 2I_0 \left(1 + \cos\left(kx \sin(\alpha) + \frac{2\pi \Delta OPL}{\lambda_L}\right)\right)$$
$$\text{with} \quad \Delta OPL = \int_C \Delta n(s)\, ds. \tag{2}$$

The term within the cosine contains both the above-mentioned carrier contribution as well as the contribution from the gas-jet induced phase shift. The optical path length difference depends on the density distribution of the gas-jet and its associated refractive index change $\Delta n(s)$ along a path C.

2.1.1. Setup Stability

Besides the phase shift introduced by the gas-jet, disturbances like air flow, irregularities in optics and scattered laser-light add unwanted extra phase disturbances. Including these extra influences and rewriting equation (2) gives

$$I(x,y) = I_A(x,y) +$$
$$I_B(x,y) \cos\left[\varphi_c(x,y) + \varphi_s(x,y) + \varphi_d(x,y)\right]. \tag{3}$$

The CCD-chip defines the x,y-plane. I_A is the background and I_B the local amplitude of the fringe function, which may vary in the case of a non-uniform illumination. φ_c is the carrier phase and φ_s is the signal phase, they correspond

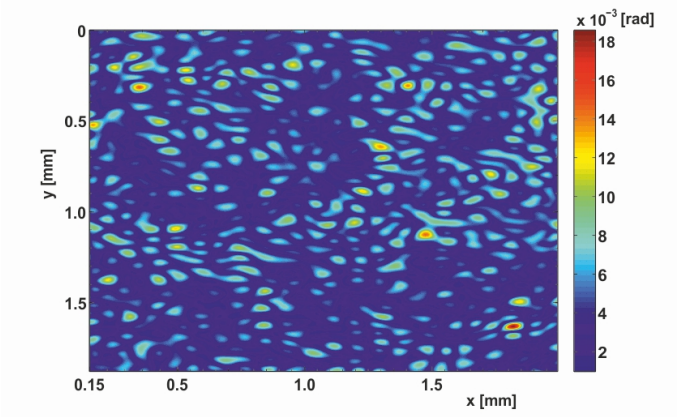

Figure 2: Standard deviation map over 30 measurements. The phase map was constructed when no jet was present and shows the stability of the setup.

to the first and second part within the cosine of equation (2) respectively. φ_d contains all disturbances that do not come from the static fringe pattern or the gas jet. The setup has been optimised to keep φ_d as low as possible. This is achieved by using active vibration isolation of the optical table, encasement to minimize air-turbulences and dust scattering and placing optics away from the imaging plane so unwanted scattering from optics defects do not image to the camera plane.

Figure 2 shows a noise map of the setup. This map is constructed by taking measurements under experimental conditions but without a gas-jet present. Ideally, every single measurement should render the exact same phase map. Small fluctuations in setup stability introduce phase disturbances φ_d for every shot. The shot-to-shot standard deviation is a measure for the noise in the setup. Overall, the average standard deviation is 3.9×10^{-3} rad, well below the shift expected for the gas-jet targets.

2.2. Data processing

After acquisition of the images, we further process the data to reconstruct the gas density profile. This is done in two steps: Phase retrieval (section

2.2.1), followed by gas density reconstruction, by Abel-inversion or tomographic reconstruction (section 2.2.2).

2.2.1. Phase retrieval

A typical interferogram can be seen in figure 3(a). This image contains all the information as expressed in eq. (3). Since only the phase shift φ_s is of interest, data-processing is required to extract this information. Using the Fourier-transform method [9] we transform the image into the Fourier domain to filter the phase information. Rewriting eq. (3) in the frequency domain gives:

$$\hat{I}(f_x, f_y) = \hat{I}_A(f_x, f_y) + \hat{I}_C(f_x - f_{c,x}, f_y - f_{c,y}) + \hat{I}_C^*(f_x + f_{c,x}, f_y + f_{c,y}), \quad (4)$$

where the hat denotes the Fourier transform and the asterisk superscript denotes the complex conjugate. At this stage a frequency filter is applied to the Fourier transform. Only the $\hat{I}_C(f_x - f_{c,x}, f_y - f_{c,y})$ part is selected. A two-dimensional representation of this process is shown in figure 4. By defining the range of the filter, noise components outside this range are filtered out.

Performing a back Fourier transformation over the selected filter gives an intensity according to equation (3). The background variation is contained in the real part and the phase in the imaginary part. The phase information is extracted from I_C by:

$$\tan^{-1} \frac{\Im\left[I_C(x,y)\right]}{\Re\left[I_C(x,y)\right]} = (\varphi_c + \varphi_s + \varphi_d)(x,y). \quad (5)$$

To remove the carrier phase component the same process is also performed on a reference shot where no gas-jet is present, which renders an interferogram which does not contain a φ_s term. By subtracting the reference shot phase from the signal shot phase, the φ_c term is removed from equation (5). Figure 3(b) shows the resulting phase map corresponding to the interferogram from figure 3(a) acquired by this method.

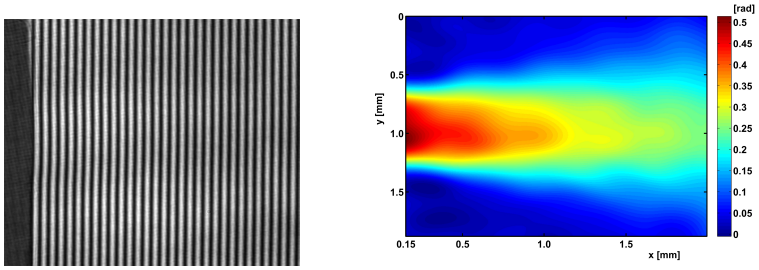

(a) Interferogram. The nozzle can be partly seen on the left.

(b) Induced phase shift. Acquired over 25 averages

Figure 3: Interferogram and corresponding phase shift induced by a helium gasjet produced by a 0.75 mm Mach 4.8 de Laval nozzle with a backing pressure of 70.5 bar.

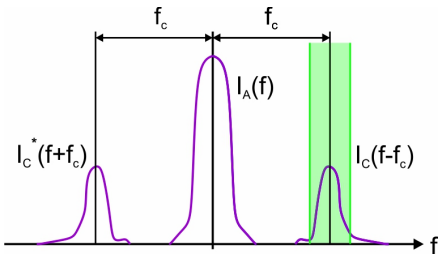

Figure 4: Fourier spectrum with separated contributions. The green area represents a possible filter range.

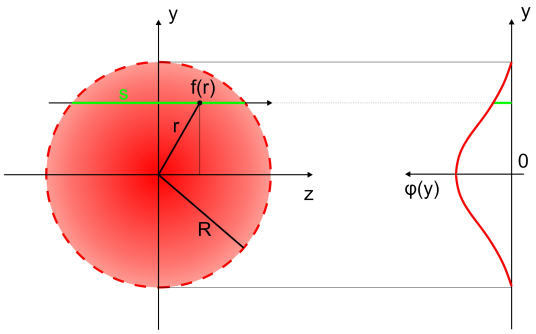

Figure 5: Abel Transformation.

2.2.2. Gas density reconstruction

In experiment, the signal laser beam travels through the three-dimensional (3-D) gas jet and projects the gas-density information on the two-dimensional (2-D) CCD-chip. To obtain a 3-D gas-jet density map we either perform an Abel-inversion or use tomographic back-projection.

For axisymmetrical gas-jets, Abel inversion can be used. In this case, we take a phase shift measurement under a single angle and reconstruct the gasjet under assumption of cylindrical symmetry. Figure 5 shows the Abel transformation from a 3-D gas-jet to 2-D projection. The measured phase shift at a certain distance x from the nozzle $\varphi(y)$ is the integral according to equation (2) along the optical path s. Via the inverse Abel transform we can translate $\varphi(y)$ into $f(r)$, which is a function related to the gas density at a distance r from the nozzle centre. The analytical solution of the inverse Abel transform is [10]:

$$f(r) = -\frac{1}{\pi}\int_y^R \frac{d\varphi(y)}{dy}\frac{dy}{\sqrt{r^2-y^2}}dr. \tag{6}$$

Since a full analytical solution is not possible for data-analysis we use a numerical Abel inversion. Results presented in this paper are processed with the **I**nterferometrical **D**ata **E**valuation **A**lgorithms (IDEA) software developed by the Graz University of Technology using the f-interpolation method [11].

For gas-jets that are not axisymmetric, we use a tomographic reconstruction algorithm. By taking different 2-D projections under multiple angles the 3-D gas-jet can be reconstructed using the Fourier slice theorem: [12]

$$f(x,y) = \int_0^{\pi} \int_{-\infty}^{+\infty} \hat{I}(k_r,\theta)|k_r| e^{i2\pi k_r x cos(\theta)+ysin(\theta)} dk_r d\theta, \tag{7}$$

with $\hat{I}(k_r,\theta)$ the Fourier transform of the measured projection in polar coordinates. $|k_r|$ is the filter used that weights the spatial frequency contributions in the projection. Using this filter prevents blurring of the reconstructed image. In our analysis we use a Hann-filter [13].

The function f that is obtained either by Abel inversion or tomography is related to the refractive index of the gas by:

$$f(r) = \frac{2\pi}{\lambda}\left(\eta(r) - 1\right). \tag{8}$$

The index of refraction η is dependent on the gas density n and the laser wavelength λ according to the Lorentz-Lorenz equation [14–16].

$$\frac{\eta(\lambda)^2 - 1}{\eta(\lambda)^2 + 2} = \frac{n\alpha(\lambda)}{3\epsilon_0}, \tag{9}$$

with α the polarizability of the gas and ϵ_0 the permittivity of free space. For $\eta \approx 1$, the gas density can be approximated by

$$n \approx \frac{2\epsilon_0}{\alpha(\lambda)}\left(\eta(\lambda) - 1\right). \tag{10}$$

Table 1 gives values for η and α for various gases. With these values and equation (10) the gas density can be calculated from the Abel transformed measurements.

A helium jet of 0.75 mm with a gas density of 7×10^{18} cm^{-3} gives an expected phase shift of only 6×10^{-2} radians. The same jet operated with the same density argon or nitrogen will give a considerably larger phase shift

Table 1: Polarizability and the index of refraction of several gases at 273K, p = 1 atm. and a probe wavelength of $\lambda = 633$ nm. Values of η from [17]. Values for α according to eq. (9).

	$\eta - 1(10^{-5})$	$\alpha(10^{-41}$ F m$^2)$
He	3.492	2.300
Ar	28.12	18.52
H_2	13.88	9.143
N_2	29.79	19.62

of around 0.5 radians. The stability of our setup (section 2.1.1) allows us to perform direct measurements on helium gas-jets.

3. Results

The setup (figure 1) was used to analyse multiple nozzles that are intended for use in LWFA. For axisymmetrical nozzles a comparison is made between determining the gas density profile by Abel inversion and using tomography. A direct comparison between a nozzle driven by argon and helium is made. A slit nozzle with a shock-front induced density gradient is analysed using tomography.

3.1. Comparison between Abel inversion and Tomography

For comparison between Abel inversion and Tomography a conical Mach 4.8 de Laval nozzle [18] is used. The nozzle has a throat of 0.25 mm and a nozzle exit diameter of 0.75 mm. This nozzle is designed to provide a flat-top density profile with steep gradients and has been analysed as such [19, 20]. After extensive use in LWFA experiments this nozzle has degraded and a defect was suspected. Figure 6 shows analysis of this nozzle by both measurement methods. Both methods show that the nozzle has degraded to the point where it does not have a steep-gradient flat-top profile. But because the Abel inversion method assumes axisymmetry, this method is not able to detect the asymmetry in the density profile that clearly shows up in the tomographic analysis.

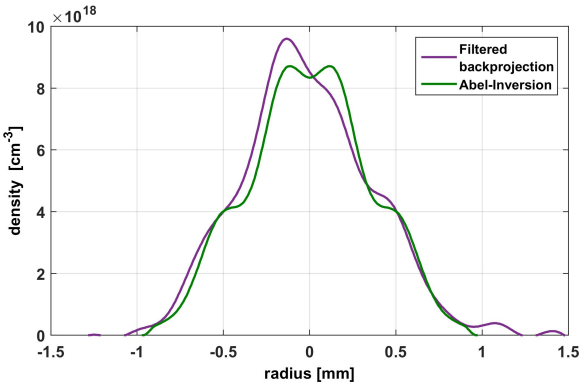

Figure 6: Comparison between Abel-inversion and tomography at a degraded conical Mach 4.8 de Laval 700 μm above the nozzle exit. Argon, 20 bar backing pressure. Line-out over the nozzle centre for the tomography, Abel-inversion relies on centro-symmetry.

What has to be considered though, is that for tomographic analysis the gas-jet target has to be rotated to acquire images under multiple images, which is not necessary for Abel inversion analysis. Therefore, especially in the case of on-site analysis of gas-jet targets during LWFA experiments where the degradation of the gas-nozzle has to be monitored, Abel-inversion analysis can be favourable due to the simplification of the setup.

3.2. Comparison between Argon and Helium gas

Although LWFA experiments are generally performed on helium jets, the nozzles used to provide these jets are often characterised using argon gas. The reason for this is the higher refractive index of argon compared to helium (Table 1), which will result in a corresponding larger phase shift, thus relaxing the sensitivity requirements of the interferometry setup. Argon and helium are both mono-atomic gases with the same adiabatic index. Theory and simulation performed for de Laval type nozzles predict different nozzle exit velocities for argon and helium, but no major differences in gas density [18, 21].

To test whether this assumption can be applied, we did gas density measurements on a nozzle driven by both argon and helium. The nozzle used for

this comparison is a Sourcelab SL-NOZ-SS Mach ∼5.5 nozzle with a throat size of 0.5 mm and an exit size of 2 mm.

Tomography depends on measurements under multiple angles for which we assume that the gas-jet is equal for every shot. Therefore the shot-to-shot stability of the jet is important. This is also important for LWFA where a stable acceleration medium is required. To evaluate the shot-to-shot stability of the SL-NOZ-SS target we took ten different measurements at one minute intervals with the gas-jet driven at 20 bar argon. One angle is considered and stability is evaluated on the acquired phase maps. We consider the inner area of the jet (± 0.25 mm around the centre and up to two mm from the nozzle exit). The average shot-to-shot relative standard deviation is 1.6%. This is stable enough not to add any relevant error to the tomographic reconstruction.

Figure 7 shows the 2-D gas density maps at 1 mm above the nozzle exit for both argon and helium at 40 bar backing pressure. The density maps have been acquired by tomographic reconstruction using 20 angles. The reconstruction shows an asymmetry, which we believe arrives from an irregularity of the nozzle or from an imperfect alignment of the nozzle on the valve. Note that we can only diagnose this asymmetry because of the use of tomographic reconstruction.

Figure 8 shows line-outs for different backing pressures for both argon and helium. The shaded area around the measurement line shows the uncertainty and includes gas-jet stability as mentioned above as well as an analysis uncertainty. The analysis uncertainty has been determined by processing a zero-measurement without gas-jet present (section 2.1.1) that has been acquired under experimental conditions. This zero-measurement is processed using the same procedure as used for gas-jet data, including tomographic reconstruction. The maximum phase error found in the reconstruction is taken as the analysis uncertainty. Taking refractive indexes of both gases into account, this results in an absolute gas density uncertainty of $1.95 \times 10^{17} \mathrm{cm}^{-3}$ for argon and $1.58 \times 10^{18} \mathrm{cm}^{-3}$ for helium.

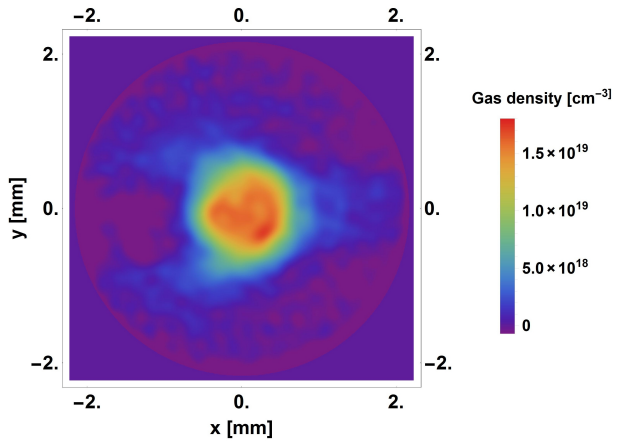

(a) Helium gas density profile

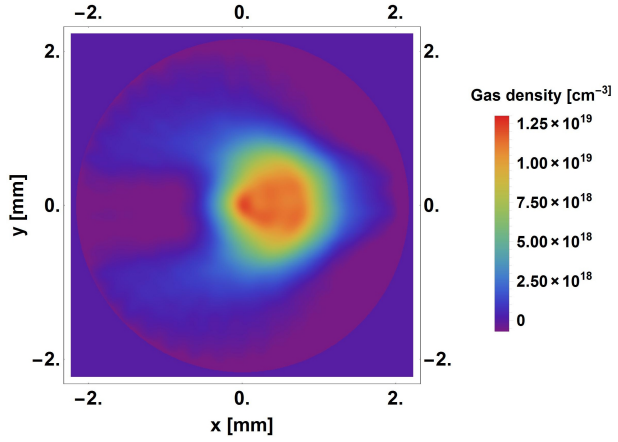

(b) Argon gas density profile

Figure 7: 2-D Gas density profile of a 0.5 mm throat, 2 mm exit Mach 5.5 nozzle. 1 mm above the nozzle exit, obtained by tomographic reconstruction. Driven by both Argon and Helium gas at 40 bar backing pressure.

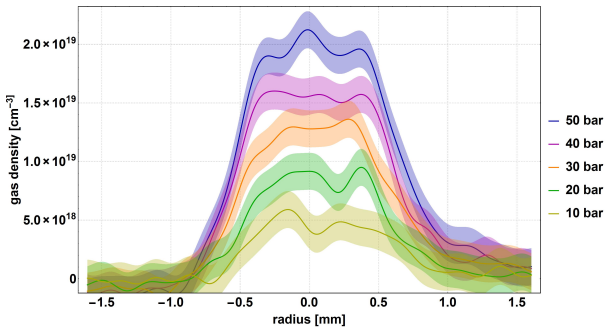

(a) Helium gas density profile.

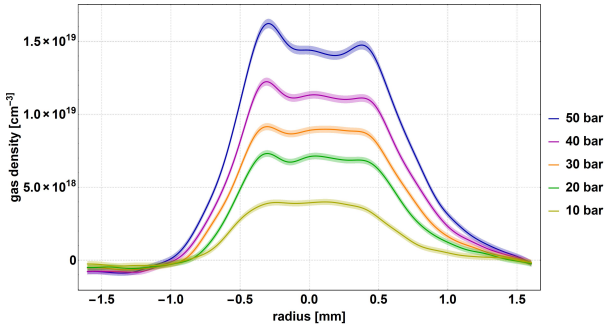

(b) Argon gas density profile

Figure 8: Gas density line-outs of a 0.5 mm throat, 2 mm exit opening Mach 5.5 nozzle. 1 mm above the nozzle exit, obtained by tomographic reconstruction. Driven by both Argon and Helium gas. The area around the solid line indicates the measurement uncertainty.

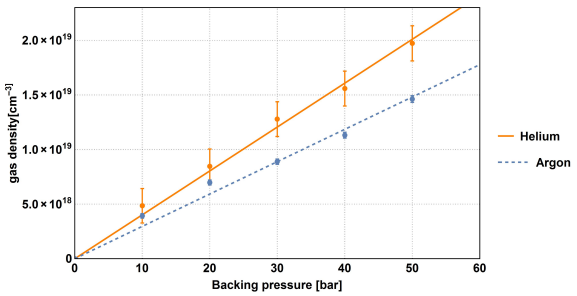

Figure 9: Average gas density at the jet centre for different backing pressures with corresponding linear fits

Figure 9 shows the average gas densities around the centre (±0.3 mm) of the jet together with a linear fit for both argon and helium. There is a clear difference between the densities obtained with both gases. In this specific case one needs apply a correction factor of 1.36 (±10%) to convert a density measurement performed on argon to the helium gas density.

3.3. Tomography of a slit nozzle

For longer LWFA interaction lengths, larger gas nozzles are required. To minimize the gas load inside the interaction chamber we developed a Mach 7 slit-nozzle with a nozzle exit of 5x1 mm^2 and a throat size of 900x220 μm^2. Because this nozzle does not posses centrosymmetry, it can only be analysed by tomography. Figure 10 shows the analysis of this nozzle. The nozzle shows a steep-gradient profile with a 3.1 mm long plateau.

Using the supersonic characteristics of this slit-nozzle, we introduced a knife-edge induced shock-wave density gradient to the slit nozzle. Figure 11 shows the resulting density profile. The density profile features two distinct regions: A shock front region with an increased density and a plateau region where the density is constant over 2.5 mm. Such a target can be interesting for a two-stage LWFA experiment, where the shock region acts as an injection stage and the flat-top as a acceleration stage. Experiments on shock-wave targets have already shown improved stability and reproducibility compared to normal gas-jet targets

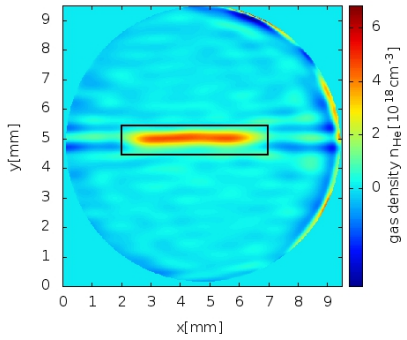

Figure 10: Tomographic analysis of a 5x1 mm^2 slit nozzle at 700 μm above the nozzle. Density map. The black square indicates the nozzle exit. Helium, 20 bar backing pressure.

[22].

4. Conclusion

We have shown that we can analyse gas-jet targets for LWFA by laser interferometry. With a setup with noise only in the 4 x 10^{-3} rad range enables us to measure very small phase shifts, enabling us to measure helium gas-jets without having to rely on higher refractive gases such as argon or nitrogen.

We compared Abel inversion and tomographic analysis of a damaged axisymmetrical nozzle and show that tomography reveals defects that will not show up with Abel inversion. With tomography we are also able to analyse slit nozzles and shock waves induced into gas-jets. In a direct comparison between helium and argon jets we have shown that it cannot be assumed that a nozzle operated with helium gives the same gas density as when operated with argon.

Acknowledgements

J.P.C. acknowledges LA3NET, which has received funding from the European Unions Seventh Framework Programme for research, technological development and demonstration under grant agreement no 289191.
Partially funded by EUCARD2 under Grant Agreement number 312453.

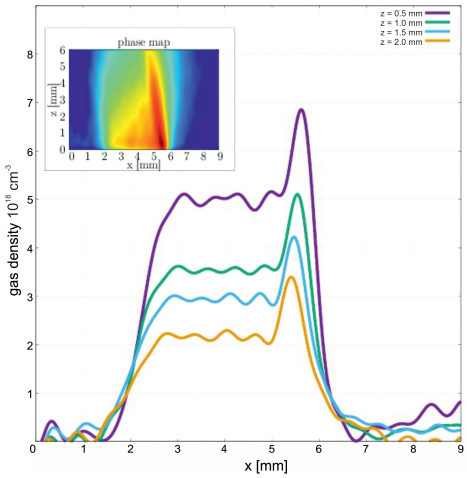

Figure 11: Density profile of slit nozzle with knife-edge at different distances from the knife. The inset shows the filtered phase image perpendicular to the long axis. Helium, 40 bar backing pressure.

References

[1] T. Tajima, J. M. Dawson, Laser electron accelerator, Phys. Rev. Lett. 43 (4) (1979) 267–270. doi:10.1103/PhysRevLett.43.267.

[2] K. Nakajima, T. Kawakubo, H. Nakanishi, A. Ogata, Y. Kato, Y. Kitagawa, R. Kodama, K. Mima, H. Shiraga, K. Suzuki, T. Zhang, Y. Sakawa, T. Shoji, Y. Nishida, N. Yugami, M. Downer, D. Fisher, B. Newberger, T. Tajima, A proof-of-principle experiment of laser wakefield acceleration, Phys. Scripta 1994 (T52) (1994) 61.
URL http://stacks.iop.org/1402-4896/1994/i=T52/a=009

[3] W. P. Leemans, a. J. Gonsalves, H.-S. Mao, K. Nakamura, C. Benedetti, C. B. Schroeder, C. Tth, J. Daniels, D. E. Mittelberger, S. S. Bulanov, Et Al., Multi-GeV Electron Beams from Capillary-Discharge-Guided Subpetawatt Laser Pulses in the Self-Trapping Regime, Phys. Rev. Lett. 245002 (December) (2014) 1–5. doi:10.1103/physrevlett.113.245002.

[4] K. Schmid, L. Veisz, Supersonic gas jets for laser-plasma experiments, Rev. Sci. Instrum. 83 (5) (2012) 053304. doi:10.1063/1.4719915.
URL http://link.aip.org/link/RSINAK/v83/i5/p053304/s1&Agg=doi

[5] V. Malka, C. Coulaud, J. P. Geindre, V. Lopez, Z. Najmudin, D. Neely, F. Amiranoff, Characterization of neutral density profile in a wide range of pressure of cylindrical pulsed gas jets, Rev. Sci. Instrum. 71 (6) (2000) 2329. doi:10.1063/1.1150619.
URL http://scitation.aip.org/content/aip/journal/rsi/71/6/10.1063/1.1150619

[6] N. Lemos, N. Lopes, J. M. Dias, F. Viola, Design and characterization of supersonic nozzles for wide focus laser-plasma interactions., Rev. Sci. Instrum. 80 (10) (2009) 103301. doi:10.1063/1.3233895.
URL http://www.ncbi.nlm.nih.gov/pubmed/19895054

[7] B. E. A. Saleh, M. C. Teich, Fundamentals of Photonics, Wiley-Interscience Publication, 1991.

[8] G. Pretzier, H. Jager, T. Neger, High-accuracy differential interferometry for the investigation of phase objects, Meas. Sci. Technol. 4 (6) (1993) 649–658. doi:10.1088/0957-0233/4/6/003.
URL http://stacks.iop.org/0957-0233/4/i=6/a=003?key=crossref.9b21243e281202ed275ab8ef21daed5f

[9] M. Takeda, H. Ina, S. Kobayashi, Fourier-transform method of fringe-pattern analysis for computer-based topography and interferometry, J. Opt. Soc. Am. 72 (1) (1982) 156–160. doi:10.1364/JOSA.72.000156.
URL http://www.opticsinfobase.org/abstract.cfm?URI=josa-72-1-156

[10] M. Hipp, P. Reiterer, User Manual for IDEA 1.7, Institut fur Experimental Physik, Technische Universitat Graz, chapter 3.6; Abel Inversion (July 2003).

[11] Idea - interferometric data evaluation algorithms, software for fringe analysis and phase data reduction, accessed: 2015-09-22.
URL http://www.optics.tugraz.at/idea/idea.html

[12] A. C. Kak, M. Slaney, Principles of Computerized Tomographic Imaging, Society of Industrial and Applied Mathematics, 2001.

[13] F. J. Harris, On the use of windows for harmonic analysis with the discrete fourier transform, Proc. IEEE 66 (1) (1978) 51–83. doi:10.1109/PROC.1978.10837.

[14] E. Wolf (Ed.), Progress in Optics, Vol. 43, Elsevier Science, 2002.

[15] L. Lorenz, Über die refractionsconstante, Ann. Phys. 11 (1880) 70–103.

[16] H. A. Lorentz, Über die beziehung zwischen der fortpflanzungsgeschwindigkeit des lichtes und der körperdichte, Ann. Phys. 9 (1880) 641–645.

[17] M. J. Weber, Handbook of Optical Materials, CRC Press, 2002.

[18] T. A. W. Wolterink, High-gradient gas-jet targets for laser wakefield acceleration, Master's thesis, University of Twente (April 2011).

[19] J. P. Couperus, Laser wakefield acceleration in the nonlinear bubble regime and gas-jet target characterization, Master's thesis, University of Twente (August 2011).

[20] A. Köhler, Charakterisierung von Plasmatargets für Laser Wakefield Experimente, Master's thesis, Technische Universität Dresden (2 2013).

[21] K. Schmid, Supersonic Micro-Jets And Their Application to Few-Cycle Laser-Driven Electron Acceleration, Ph.D. thesis, Ludwig Maximilians Universität München (2009).

[22] K. Schmid, A. Buck, C. Sears, J. Mikhailova, R. Tautz, D. Herrmann, M. Geissler, F. Krausz, L. Veisz, Density-transition based electron injector

for laser driven wakefield accelerators, Phys. Rev. STAB 13 (9) (2010) 1–5. doi:10.1103/PhysRevSTAB.13.091301.
URL http://link.aps.org/doi/10.1103/PhysRevSTAB.13.091301